nature communications

Article

https://doi.org/10.1038/s41467-025-61871-2

Bioinspired Sulfo oxygen bridges optimize interfacial water structure for enhanced hydrogen oxidation and evolution reactions

Received: 4 September 2024

Accepted: 4 July 2025

Published online: 12 July 2025

Check for updates

Chengdong Yang[1,4], Yun Gao[2,4], Zhengyu Xing[3], Xinxin Shu[1], Zechao Zhuang[2], Yueqing Wang[1], Yijuan Zheng[3], Shuang Li[3], Chong Cheng[3] ✉, Dingsheng Wang[2] ✉ & Jintao Zhang[1] ✉

Uncovering the dynamic structures of water at the electrode-solution interface is crucial for various electrocatalysis processes, where water acts as a proton and electron source. However, precisely controlling the state of water on complex interfaces remains challenging. Inspired by the metalloproteins in natural enzymes, we herein demonstrate that the hydrophilic sulfo-oxygen bridging between Co and Ru sites (Co_S-SO-Ru) optimizes interfacial water structure via a favorable hydrogen-bond network, promoting hydrogen oxidation and evolution reactions. Mechanistic studies reveal that the stereoscopic sulfo-oxygen bridges enhance the connectivity of hydrogen-bond network to promote the proton transfer process via repelling cations from the electrode surface. Furthermore, electron donating Co sites reduce the surface oxophilicity of Ru to optimize the adsorption-desorption behaviors of hydroxyl, governing the timely refreshed Ru sites to enhance catalytic performances. Such bioinspired active sites offer a different pathway for the precise design of interfacial water structure to improve electrocatalysis.

The sustainable hydrogen cycle has been considered as a viable strategy to reduce the consume of fossil fuels[1,2]. Compared with proton-exchange-membrane fuel cells, anion-exchange-membrane fuel cell[3] (AEMFC) and anion-exchange-membrane water electrolysis[4,5] (AEMWE) technologies are attractive for renewable hydrogen economy[6–8], enabling the exploration of cost-effective non-platinum catalysts for efficient hydrogen evolution and oxidation reactions (HER and HOR)[9–11]. Ruthenium has been intensively investigated for HER[12,13], yet its catalytic activity for HOR is unsatisfactory due to its high oxophilicity, which leads to strong adsorption with hydroxyl groups (Ru-OH*) and blocks the active sites[14–17]. Significant efforts have been devoted to regulating the electronic structure and chemical states of Ru electrodes, aiming to balance the adsorption-desorption of reaction intermediates (e.g., H*, OH*)[18–21]. Additionally, the structures of interfacial H_2O have been considered as a crucial factor that determines the diffusion behaviors of reaction intermediates and interfacial cations[22,23]. Recent studies have shown that the water gap in the alkaline interface disrupts the hydrogen-bond network, thereby impeding the desirable hydrogen electrocatalysis due to the increased hydrogen transfer barriers[24]. Furthermore, the presence of cations can passivate the active interface and hinder electrocatalysis in seawater, where the local alkaline environments would lead to the rapid formation of insoluble precipitates[25], such as $Mg(OH)_2$ and $Ca(OH)_2$[26,27].

To regulate the interfacial H_2O structures, doping strategies with foreign atoms to construct atomic pairs and interface structures have been explored to enhance catalytic performance, but limited by weak electrostatic interactions between metallic sites and interfacial H_2O due to the insufficient hydrophilicity of metallic electrocatalysts (Fig. 1a)[19,28–31]. Alternatively, organic compounds and amphipathic

[1]Key Laboratory for Colloid and Interface Chemistry, Ministry of Education, School of Chemistry and Chemical Engineering, Shandong University, Jinan, China. [2]Department of Chemistry, Engineering Research Center of Advanced Rare Earth Materials, Tsinghua University, Beijing, China. [3]College of Polymer Science and Engineering, State Key Laboratory of Polymer Materials Engineering, Sichuan University, Chengdu, China. [4]These authors contributed equally: Chengdong Yang, Yun Gao. ✉e-mail: chong.cheng@scu.edu.cn; wangdingsheng@mail.tsinghua.edu.cn; jtzhang@sdu.edu.cn

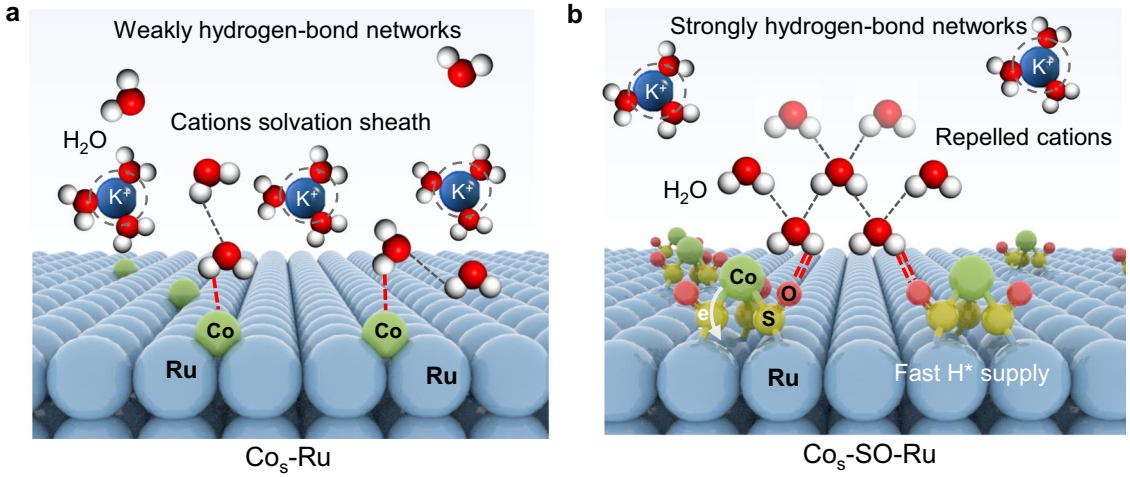

Fig. 1 | Schematic design of hydrogen-bond network in the electrode-solution interface. a Schematic illustration of Co single-atom regulated hydrogen-bond network on Ru electrodes. **b** Scheme of hydrophilic sulfo-oxygen bonds bridged Co-Ru atomic pairs for regulating interfacial hydrogen-bond network. The dotted lines represent hydrogen bonds.

molecules have been introduced to modulate the interfacial H_2O by constructing hydrogen-bond network[32–34]. However, these often result in steric hindrance, blocking the metallic active sites. Thus, precisely manipulating the dynamic configurations of interfacial H_2O at atomic scale remains a significant challenge[32,35,36]. Especially, the profound roles of interfacial microenvironments in the hydrogen catalysis on Ru electrodes are still not fully understood.

In natural enzymes, the metalloprotein structures play significant roles in regulating interfacial H_2O for the enzyme catalysis[13,37–39]. For instance, the hydrogen-bond water network found in [NiFe] and [FeFe] hydrogenases assists proton transfer and facilitates the interconversion of hydrogen and H* on metal-sulfur active centers[40,41]. Numerous biomimetic electrocatalysts have been constructed to mimic geometric structures and electronic properties of natural metalloprotein to enhance the catalysis[42–44]. However, constructing a hydrogen-bond network on these artificial electrocatalysts for efficient proton transfer has rarely been achieved. Therefore, precisely controlling interfacial H_2O configurations in heterogeneous catalytic systems through organic structures synergized metallic active sites is even more urgent and challenging for enzyme-inspired catalysts.

Inspired by the metalloproteins in the enzyme system, we anchored single cobalt atoms on ruthenium nanoclusters via sulfo-oxygen bridges, creating cobalt and ruthenium atomic pairs (Co_s-SO-Ru) to optimize interfacial water for advanced hydrogen electrocatalysis (Fig. 1b). This configuration, with its strong hydrogen-bond network and modulated chemical states of Ru sites, achieves higher HOR/HER activity and durability than Co single-atom doped Ru clusters (Co_s-Ru). Electrochemical and experimental results reveal that the interfacial water is properly regulated by the hydrophilic sulfo-oxygen bridges, repelling the interfacial cations to facilitate H* transfer and supply. Mechanistic studies suggest that the sulfo-oxygen bridging electron donating Co atomic sites would regulate the electronic structure of Ru surface to lower its oxophilicity, optimizing OH* desorption. These active sites provide important platforms for regulating catalytic environments and understanding the critical role of interfacial water in electrocatalysis. This work offers general principles that could inspire other catalytic processes, including carbon dioxide reduction and other hydrogenation reactions.

Results

Structural characterization of catalysts

With the solvothermal preparation of the cobalt-based nanoplates in the presence of $CoSO_4$ and 4,4′-bipyridine (Supplementary Figs. 1–3), the Co(Ru)-organic precursor was obtained by addition of the given amount of ruthenium salt and oxygen-functionalized carbon black. The subsequent thermal annealing led to the formation of porous carbon supported ruthenium nanoclusters with the presence of single cobalt atoms (named as Co_s-SO-Ru) (Fig. 2a, Supplementary Fig. 4). The surface functional groups of carbon black are helpful to anchor possible metal ions and the corresponding counter anion via the electrostatic interaction. The "self-sulfidation" process in the presence of the counter anion (SO_4^{2-}) from $CoSO_4$ renders the formation of sulfur-oxygen bonds and/or metal sulfide by the direct pyrolysis of Co-organic precursor (Supplementary Fig. 5). In contrast, the Co-Ru atomic pairs (Co_s-Ru) without sulfo-oxygen bonds were fabricated by employing $CoNO_3$ as Co sources (Supplementary Figs. 6, 7). X-ray diffraction (XRD) patterns of Co_s-SO-Ru and Co_s-Ru only exhibit weak peak of Ru (101) plane at around 44°, indicating the atomically dispersed Co species (Fig. 2b).

Transmission electron microscopy (TEM) and high-angle annular dark-field scanning transmission electron microscopy (HAADF-STEM) reveal the uniform dispersion of metal nanoclusters with an average size of ~2 nm on porous carbon (Fig. 2c, Supplementary Fig. 8). A small number of Co/Ru-S-C single-atom sites can be observed on the carbon support, as sulfur is not readily introduced into the carbon substrate (Supplementary Fig. 9). Instead, the high-resolution HAADF-STEM images demonstrate that the atomic cobalt preferentially disperses on Ru nanoclusters through the easy formation of metal-sulfur bridge bonds (Fig. 2d)[45]. The signal intensity profiles demonstrate the possible cobalt atoms dispersed on the periodic arrangements of Ru sites (Fig. 2e)[46,47]. Additionally, high-resolution energy dispersive X-ray spectroscopy (EDX) elemental mappings demonstrate that the Co signal is sporadically distributed across the Ru clusters, providing preliminary evidence for the atomic dispersion of Co sites in Co_s-SO-Ru (Fig. 2f, Supplementary Figs. 10,11). For the Fourier transform infrared (FT-IR) spectra (Fig. 2g), in comparison with Co_s-Ru, the new noticeable adsorption peak at 919 cm^{-1} would be attributed to the stretching vibrations of sulfo-oxygen vibration in Co_s-SO-Ru. Notably, the sulfo-oxygen bonds can be removed by the acid etching of Co_s-SO-Ru (Supplementary Fig. 12). Thus, the sulfo-oxygen bonds are not doped into carbon matrix. These results suggest that the stereoscopic sulfo-oxygen bonds would be formed on Ru nanoclusters to bridge with cobalt atoms. Such unique bridging structure would not only modulate the surface status of ruthenium, but also are involved into the hydrogen-bond networks at electrode-solution interface.

To explore the local coordination environments and electronic structure of the Co_s-SO-Ru and Co_s-Ru catalysts (Supplementary Fig. 13

https://doi.org/10.1038/s41467-025-61871-2

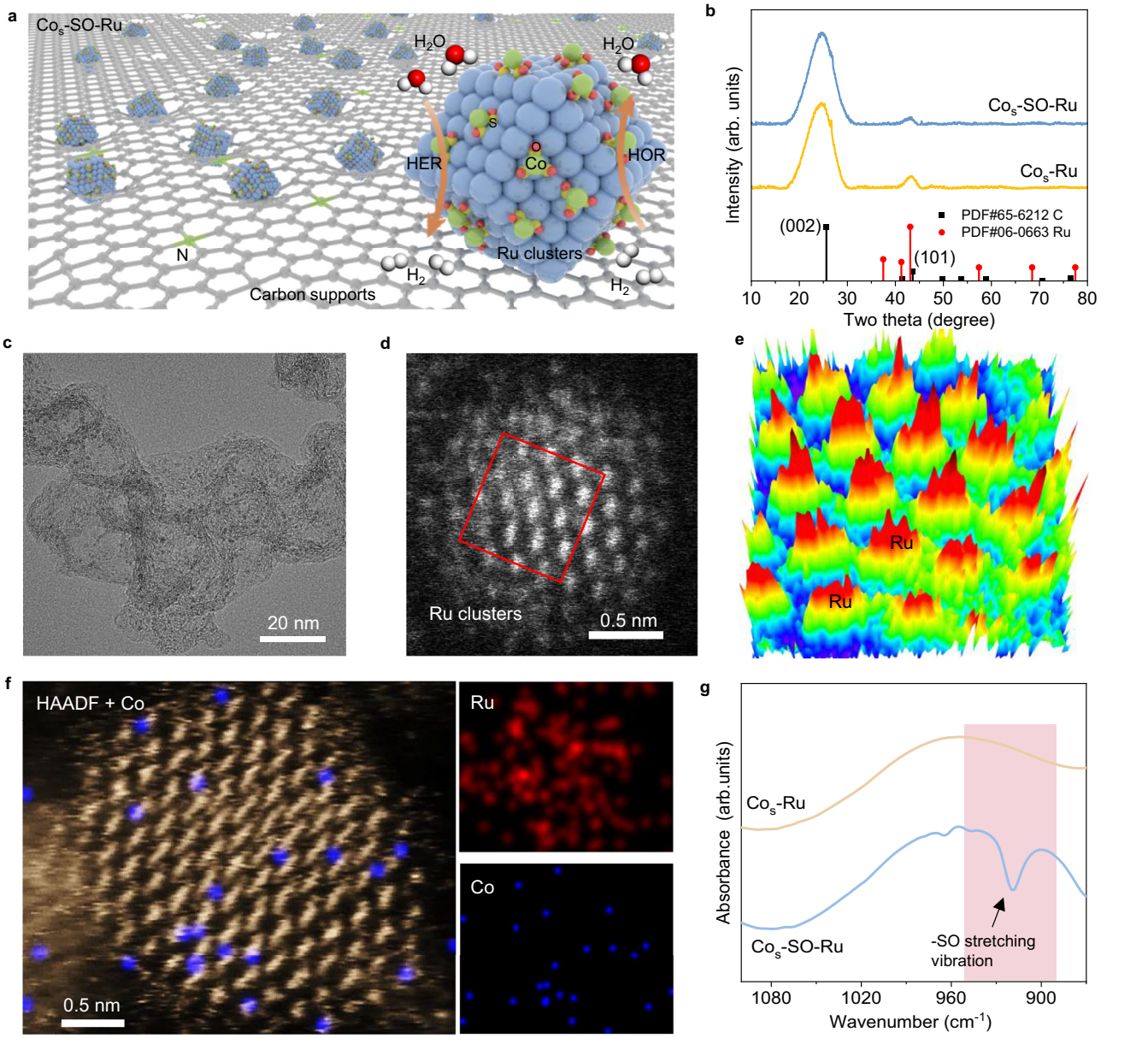

Fig. 2 | Structure characterization of sulfo-oxygen bridged Co-Ru atom sites. **a** Schematic illustration of the structure of Co$_s$-SO-Ru. **b** XRD patterns of different catalysts. **c** TEM image of Co$_s$-SO-Ru. **d** Atomic-resolution HAADF-STEM image of Co$_s$-SO-Ru and **e** corresponding plane intensity profiles labeled with red boxes in (**d**). **f** Atomic-resolution HAADF-STEM image of Co$_s$-SO-Ru and corresponding EDX mapping results of Ru and Co elements. **g** FT-IR spectra of different catalysts. Source data for (**b**, **g**) are provided as a Source Data file.

and Supplementary Tables 1, 2), the high-resolution S 2*p* X-ray photoelectron spectroscopy (XPS) spectra confirm the formation of S = O bonds (167.1 eV), which stem from the deoxygenation and reduction of the SO_4^{2-} anion via the self-sulfidation process during pyrolysis. The peaks at 161.5 and 163.3 eV can be attributed to the bonds of sulfur with Ru/Co and carbon[48] (Fig. 3a and Supplementary Fig. 14a, b), respectively. The weak binding peak demonstrates that sulfur can hardly be introduced into carbon substrate, but the coordination with cobalt would be easily formed via the atomic structure of Co-S in Co$_s$-SO-Ru. For O 1*s* spectra, the remarkable difference between Co$_s$-SO-Ru and Co$_s$-Ru confirms the formation of sulfo-oxygen bridges in Co$_s$-SO-Ru catalysts (Fig. 3b, Supplementary Fig. 14c). For high-resolution Ru 3*p* spectra, the negative shift of Ru in both Co$_s$-SO-Ru and Co$_s$-Ru is observed in comparison with Ru/C due to the electron donation to Ru in the presence of cobalt atoms (Fig. 3c, Supplementary Fig. 15). In addition, the electron donating cobalt in Co$_s$-SO-Ru shows a higher binding energy compared to that in Co_9S_8/CoO-NC obtained by direct pyrolysis of Co-organic precursor (Supplementary Figs. 16, 17). These observations suggest a strong electronic interaction with electron transfer from Co to Ru sites, leading to the low oxophilic Ru surface for the favorable desorption of intermediates adsorbed (OH*)[49].

For the Ru *K*-edge, the X-ray absorption near-edge structure (XANES) results exhibit that the absorption edge energy of Co$_s$-SO-Ru is similar to that of Ru foil (Fig. 3d, Supplementary Fig. 18), demonstrating an average valence close to Ru^0. In contrast, the XANES of Co$_s$-SO-Ru in Co *K*-edge shows a high-energy position close to Co_3O_4, possibly due to the electron donation to Ru sites (Fig. 3e). In Fourier-transforms (FT) and wavelet-transforms (WT) of k^3-weighted extended X-ray absorption fine structure (EXAFS) spectrum, the dominant bonds at ~1.99 Å for Co$_s$-SO-Ru is longer than the Ru-O bonds (1.97 Å) in RuO_2, which can be attributed to the mixture coordination of Ru-S/N with the relatively long Ru-S bonds (Fig. 3f, Supplementary Figs. 19, 20,

https://doi.org/10.1038/s41467-025-61871-2

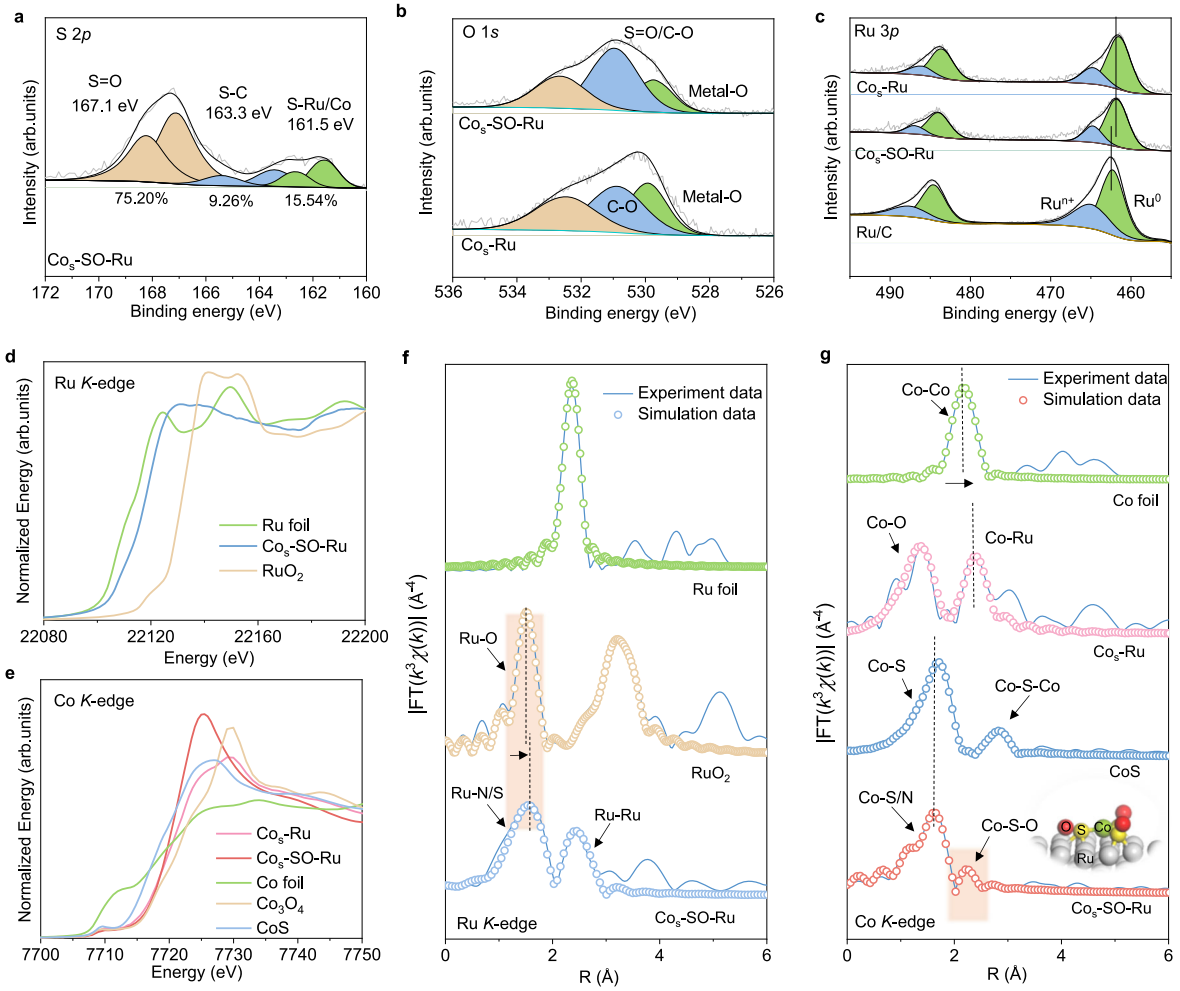

Fig. 3 | Structural analysis of Co$_s$-SO-Ru. a XPS spectra of Co$_s$-SO-Ru in S 2*p* regions. **b** XPS spectra of Co$_s$-SO-Ru and Co$_s$-Ru in O 1*s* regions. **c** XPS spectra of Co$_s$-SO-Ru and Co$_s$-Ru in Ru 3*p* regions. XANES spectra taken at **d** Ru and **e** Co *K*-edge. FT-EXAFS in R-space and corresponding fitting curves for **f** Ru foil, RuO_2, Co$_s$-SO-Ru and **g** Co foil, CoS, Co$_s$-Ru, Co$_s$-SO-Ru. All the original EXAFS data are processed without phase corrections. *R* represents the distance between the absorbing atoms and neighboring atoms, and $\chi(k)$ denotes the amplitude of the EXAFS oscillations as a function of photoelectron wavenumber *k*. Source data are provided as a Source Data file.

Supplementary Table 3). Moreover, the FT-EXAFS spectrum and corresponding WT images at the Co *K*-edge show the predominant Co-S bonds (2.23 Å) in the first coordination shell and weak Co-S-O bonds (2.80 Å) in the second coordination shell (Fig. 3g, Supplementary Figs. 21–23, and Supplementary Table 4), indicating the formation of sulfo-oxygen bonds bridged Co single-atoms. The Co-S peak in Co$_s$-SO-Ru is slightly shorter than that in CoS, which can be attributed to the formation of Co-N structures on carbon substrate (Supplementary Fig. 24, and Supplementary Table 4). No Co-Co and Co-O-Co peaks can be detected by EXAFS spectrum and WT images, strongly confirming the presence of mononuclear cobalt via sulfo-oxygen bridging with ruthenium sites in Co$_s$-SO-Ru[50].

Hydrogen electrocatalysis

The Co$_s$-SO-Ru electrocatalyst with different Ru content were analyzed in H_2-saturated aqueous 0.1 M KOH on a rotating disk electrode (Supplementary Fig. 25). As shown in Fig. 4a, the Co$_s$-SO-Ru exhibits the highest diffusion-limited current density (2.67 mA cm^{-2}) than those of Co$_s$-Ru (2.05 mA cm^{-2}), Ru/C (1.62 mA cm^{-2}), and Pt/C (1.86 mA cm^{-2}). The Co$_s$-SO-Ru-etch without Co$_s$-SO structures on the surface of Ru was also prepared via the acid treatment. The Co$_s$-SO-Ru-etch shows the lower diffusion-limited current density than that of Co$_s$-SO-Ru, indicating the profound roles of sulfo-oxygen bridging of Co and Ru sites for catalyzing HOR (Supplementary Fig. 26). Moreover, compared with Ru/C, the Co$_s$-SO-Ru exhibits stable current density at high oxidation potentials above 0.8 V, which would be contributed to the low oxophilicity of Ru sites and oxide-free catalytic surface for Co$_s$-SO-Ru.

The mass transport processes have been explored at different rotating speeds (Supplementary Fig. 27). According to the Koutecky-Levich equation, the slope for HOR at Co$_s$-SO-Ru electrode is determined as 4.51 cm^2 mA^{-1}s$^{-1/2}$, similar to the theoretical value (4.87 cm^2 mA^{-1}s$^{-1/2}$). The calculated number of transferred electrons is 2.09, and the extra transferred electrons may be attributed to the slight oxidation of catalysts. The Co$_s$-SO-Ru also exhibits higher kinetic current density (j_k) than that at the Co$_s$-Ru electrode at different oxidation potentials, indicating the promoted kinetics (Fig. 4b). Meanwhile, the exchange current density (j_0) of different samples is obtained by the fitting of micro-polarization region. The Co$_s$-SO-Ru shows a higher j_0 (3.51 mA cm^{-2}) and normalized mass activity ($j_{k,m}$) (3.44 A mg$_{metal}^{-1}$) than those of Co$_s$-Ru and other state-of-the-art electrocatalysts (Fig. 4c, Supplementary Tables 5, 6), thus evidencing the enhanced intrinsic activity. The j_0 was further normalized by electrochemical active surface area (ECSA) obtained via Cu

https://doi.org/10.1038/s41467-025-61871-2

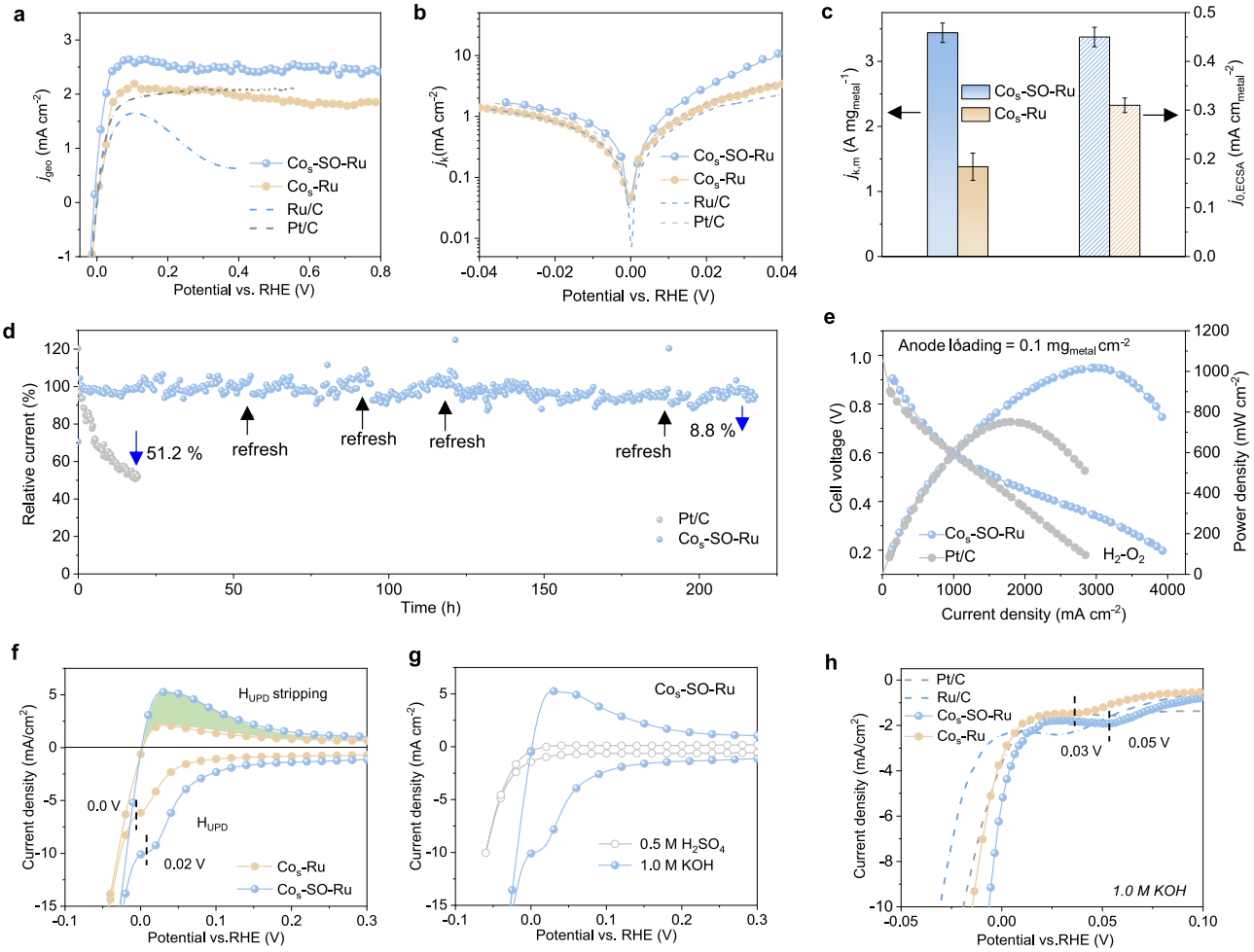

Fig. 4 | Electrocatalytic analysis. a HOR curves of different catalysts in H_2-saturated 0.1 M KOH with real-time iR correction of 31.0 ohms. **b** Calculated Tafel plots of the kinetic current density (j_k). **c** Comparison of kinetic mass activity ($j_{k,m}$) with an overpotential of 50 mV and exchange current density ($j_{0,\ ECSA}$) normalized by ECSA. **d** Long-term stability test of different catalysts at 0.1 V. **e** Polarization and power density curves of AEMFCs using different catalysts as anode. Test conditions: Using Co$_s$-SO-Ru or Pt/C (0.1 mg$_{Ru}$ cm^{-2}) as anode and Pt/C (0.4 mg$_{Pt}$ cm^{-2}) as cathode with H_2 and O_2 flow rate of 1.0 L min^{-1}. The cell, anode, and cathode humidifier temperatures are 80, 77, and 79 °C, respectively; back pressures were symmetric at 200 kPag for both sides. **f, g** Comparison of H* adsorption behavior of different catalysts in acid and alkaline conditions. **h** HER curves of different catalysts in 1.0 M KOH with real-time iR correction of 4.4 ohms. Source data are provided as a Source Data file.

underpotential deposition (Cu-UPD) tests (Fig. 4c, Supplementary Fig. 28). The Co$_s$-SO-Ru catalyst achieves a $j_{0,\ ECSA}$ of 0.45 mA cm$_{metal}^{-2}$, indicating the comparable specific activity compared to previously reported catalysts (Fig. 4c, Supplementary Table 7). This notable catalytic performance would be contributed to the unique bridging structure for modulating the interfacial H_2O.

The long-term stability was examined by chronoamperometry method at 100 mV without iR corrections. The current density of Co$_s$-SO-Ru exhibits only a slight decrease of 8.8% after 200 h, thus confirming the outstanding durability compared to other state-of-the-art catalysts (Fig. 4d, Supplementary Table 8). The TEM and HAADF-STEM images reveal that the spent catalyst retains similar structures and nearly unchanged size of Ru clusters (~2 nm) compared with the pristine Co$_s$-SO-Ru (Supplementary Figs. 29,30), demonstrating the stable structure. The EDX mapping exhibits the homogenous dispersion of sulfur and oxygen atoms in Co$_s$-SO-Ru after 200 h of operation (Supplementary Fig. 31). The XPS analysis further confirms that the S = O and S-Ru/Co bonds remain well-preserved (Supplementary Fig. 32), indicating the structural robustness of S = O bridges in Co$_s$-SO-Ru. Additionally, the Ru sites also maintain a stable valence state under the oxidation potential after 200 h of testing (Supplementary Fig. 33). Overall, these experimental results confirm the stable chemical states of Co$_s$-SO-Ru. Encouraged by the good HOR catalytic performance of Co$_s$-SO-Ru, the membrane electrode assembly was fabricated using Co$_s$-SO-Ru or Pt/C (0.1 mg$_{Ru}$ cm^{-2}) as the anode and Pt/C (0.4 mg$_{Pt}$ cm^{-2}) as the cathode. Figure 4e illustrates that the Co$_s$-SO-Ru achieves a peak power density of 1.02 W cm^{-2} at a current density of 2.96 A cm^{-2}, outperforming the performance of the Pt/C anode, which exhibits a power density of 0.75 W cm^{-2} at 1.84 A cm^{-2}. Additionally, the Co$_s$-SO-Ru display comparable stability with a 0.1 V voltage decrease after 40 h of operation (Supplementary Fig. 34), demonstrating the great potential for practical applications.

The hydrogen binding energy (HBE) has been considered an important factor of interfacial water to regulate electrocatalytic activities. Therefore, the HBE of different catalysts was analyzed by the hydrogen underpotential deposition (H_{UPD}) through cyclic voltammetry (CV) curves. As shown in Fig. 4f, the Co$_s$-SO-Ru exhibits well-resolved H_{UPD} peak and stripping peak in comparison to Co$_s$-Ru, thus indicating the enhanced adsorption of active hydrogen species (H*). Interestingly, the absence of H_{UPD} peak in acid condition reveals that the free H_3O^+ ions in solution are not easily adsorbed as active species at a relatively low potential (Fig. 4g). Therefore, the obvious adsorption and stripping currents at Co$_s$-SO-Ru electrode in alkaline conditions would be attributed to the hydrogen adsorption and desorption

via the favorable hydrogen-bond network of water and the subsequent formation of adsorbed hydrogen ($H_2O + e^- \rightarrow H^* + OH^-$), possibly boosting the electrocatalytic hydrogen conversion process.

The electrocatalytic performance for hydrogen evolution was evaluated in alkaline condition with real-time iR correction (details in Methods), and the overpotential of 6 mV to deliver the current density of 10 mA cm^{-2} at the Co_s-SO-Ru electrode is lower than those of commercial Pt/C (20 mV), Ru/C (32 mV), and Co_s-Ru (15 mV), thus suggesting the outstanding HER activities (Fig. 4i, Supplementary Figs. 35, 36). Moreover, the easy hydrogen adsorption at 0.05 V of Co_s-SO-Ru before HER in 1.0 M KOH indicates the favorable proton supply process. The Tafel slope and overpotential analysis further highlight the favorable kinetics of HER, comparable to those of many previously reported Ru-based materials (Supplementary Figs. 37, 38, Supplementary Table 9). To investigate the intrinsic HER activity of different catalysts, the mass activity and turnover frequency (TOF) were calculated on the basis of the contents of noble metals. The mass activity of Co_s-SO-Ru is up to 13.19 A mg_{Ru}^{-1} with a potential of −0.1 V, which is two-times higher than that of Co_s-Ru (6.35 A mg_{Ru}^{-1}) (Supplementary Figs. 39, 40). Additionally, the Co_s-SO-Ru electrode also demonstrates outstanding stability with slight potential decay over 20 h (Supplementary Fig. 41). Overall, the Co_s-SO-Ru exhibits better HER catalytic performance in terms of overpotential, Tafel slope, mass activity, and TOF in comparison with Co_s-Ru (Supplementary Fig. 42). These results unveil that the sulfo-oxygen bridged Co-Ru pair sites can greatly enhance the intrinsic hydrogen-evolving activity.

In situ spectroscope characterizations

To better explore the interfacial microenvironments of Co_s-SO-Ru in alkaline conditions, the attenuated total reflection surface-enhanced infrared adsorption spectroscopy (ATR-SEIRAS) was performed to detect the binding behaviors of different intermediates (Supplementary Figs. 43, 44). The interfacial configuration of water (H_2O^*) was monitored on the basis of the -OH stretching mode (ν_{OH}^*). The SEIRAS signal centered at around 3200, 3350, and 3600 cm^{-1} can be assigned to strongly bound water, intermediately bound water, and free water, respectively[51]. For Co_s-Ru electrode, the major peaks can be assigned to the intermediately bound water (3400 cm^{-1}) and free water (3598 cm^{-1}) at different applied potentials, indicating the weak hydrogen-bond network (Fig. 5a, c). In contrast, the Co_s-SO-Ru electrode exhibits that the intensified peaks at 3219 and 3355 cm^{-1} in the potential range from 0.1 to −0.30 V are ascribed to the strongly bound water, suggesting the strengthen hydrogen-bond network in electrochemical double layer[52] (Fig. 5b–d, Supplementary Fig. 45). This strongly bound water would promote the proton hopping from bulk solution to electrode-solution interface via the high connectivity of hydrogen-bond networks, thus enhancing reaction kinetics of hydrogen catalysis. This standpoint is also demonstrated by heavy adsorption of H_{UPD} on the surface of Co_s-SO-Ru at a relative low potential (0.15 V vs. RHE). Moreover, the OH* diffusion process would also be promoted through the hydrogen-bond networks[32,53], which accounts for the stable current density under high oxidation potential.

The dynamic structures of hydrogen-bond network were analyzed under different reaction times. Typically, the intensity of ν_{OH}^* bond at 3359 cm^{-1} with a slight redshift is increased with the increasing reaction time from 2 to 10 min, suggesting the intermediately hydrogen-bound H_2O in the electrode-water interface (Fig. 5e). These intermediately hydrogen-bond H_2O may timely replenish the strong hydrogen-bond network. As illustrated in Fig. 5f, the hydrophilic sulfo-oxygen bridges build strong hydrogen-bond networks by the formation of -S = O ···H_2O bonds to promote the proton supply and hydroxyl diffusion processes in the electrode-electrolyte interface. Consequently, the Co_s-SO-Ru exhibits the outstanding hydrogen conversion kinetics under both oxidation/reduction potentials. At the alkaline interface, a significant number of cations are present to counterbalance the high density of negative charges, causing them to become partially desolvated[19]. The interaction between these alkaline cations and the electrode surface compensates for the loss of solvation interaction, disrupting the connectivity of hydrogen-bond networks (Fig. 1a). During seawater splitting, the accumulation of cations, such as Ca^{2+} and Mg^{2+}, would also lead to the rapid formation of insoluble precipitates at the electrode-liquid interface, suppressing the catalytic activity. To address these challenges, the HER catalytic performance of Co_s-SO-Ru was tested in seawater. The Co_s-SO-Ru exhibited negligible activity decay after 80,000 s, with only a 24 mV increase in overpotential, indicating its anti-poisoning capability for seawater splitting (Supplementary Figs. 46, 47). Under seawater conditions, the stereoscopic -S = O bridges in Co_s-SO-Ru enable the formation of a strongly bonded interfacial hydrogen-bond network, which would alleviate the accumulation of Ca^{2+} and Mg^{2+} cations at the active interface. This reduction in cation concentration at the electrode-liquid interface prevents the formation of insoluble precipitates (e.g., $Ca(OH)_2$, $Mg(OH)_2$), thus enhancing the long-term catalytic stability of the Co_s-SO-Ru electrode. Additionally, the sulfo-oxygen bridged Co atoms would decrease the oxophilicity of Ru nanoclusters, facilitating the desorption of OH* from Ru and avoiding precipitate formation on Ru electrodes.

Mechanism investigation

The first-principle density functional theory (DFT) calculation was further conducted to investigate the origins of catalytic behaviors of Co_s-SO-Ru. According to the atomic arrangement information, the theoretical structure was proposed (Supplementary Fig. 48 and Supplementary data 1). For comparison, the model of Co atomic sites modified Ru clusters was also constructed. The charge density difference results demonstrate the obvious electron accumulation on Ru clusters in both Co_s-SO-Ru and Co_s-Ru, transferred from cobalt atoms (Supplementary Fig. 49). The electron-enriched Ru surface with low oxophilicity would avoid excessive OH* occupation on Ru sites during HOR/HER process[6]. The charge density difference of H_2O^* adsorbed on different active sites was explored to understand the interfacial configurations. The strong electrostatic interaction between H_2O^* and oxygen atoms in the hydrophilic sulfo-oxygen bridge enhances the connectivity of strongly hydrogen-bond networks (Fig. 6a, b).

The HBE and H_2O binding energy (H_2OBE) are crucial descriptors for alkaline HER/HOR catalysis[54,55]. The Co_s-SO-Ru shows much higher adsorption energy to H_2O (−1.10 eV) than that of Co_s-Ru (−0.46 eV) (Fig. 6c, Supplementary Figs. 50–52), which would be attributed to the strong hydrogen-bond between H_2O and hydrophilic sulfo-oxygen bridges. Besides, due to the electron-enriched Ru sites the Gibbs free-energy diagram for hydrogen desorption on Co_s-SO-Ru exhibits a more optimal value (−0.22 eV), close to the thermo-neutral state, indicating favorable hydrogen adsorption-desorption behaviors (Fig. 6d, Supplementary Fig. 53). The favorable Ru-H* desorption process is further promoted by adjacent sulfur atoms in Co_s-SO-Ru (Supplementary Fig. 54). Overall, the DFT calculations predict that Co_s-SO-Ru features higher H_2OBE than Co_s-Ru and an optimal HBE on different sites, leading to outstanding catalytic performance (Fig. 6e, Supplementary Fig. 55).

Metallic ruthenium, with high oxophilic properties, tends to form strong Ru-OH* species at both anode and cathode potentials, making it difficult to refresh the active sites. Therefore, the adsorption behaviors of OH* have also been explored. As shown in Fig. 6f, Co_s-SO-Ru exhibits lower adsorption energy to OH* on Ru (−0.173 eV) and Co sites (0.296 eV) than those on Co_s-Ru (Ru sites (−0.519 eV) and Co sites (−0.640 eV)), confirming the weakened affinities of Ru-OH* (Supplementary Fig. 56). These results indicate that the sulfo-oxygen bridged electron donating Co atoms can efficiently regulate the electronic structures to reduce the oxophilicity of Ru sites, thus facilitating OH* desorption on surface of Co_s-SO-Ru. Moreover, the hydrogen-bond networks would also promote the hydroxyl diffusion to deliver an

https://doi.org/10.1038/s41467-025-61871-2

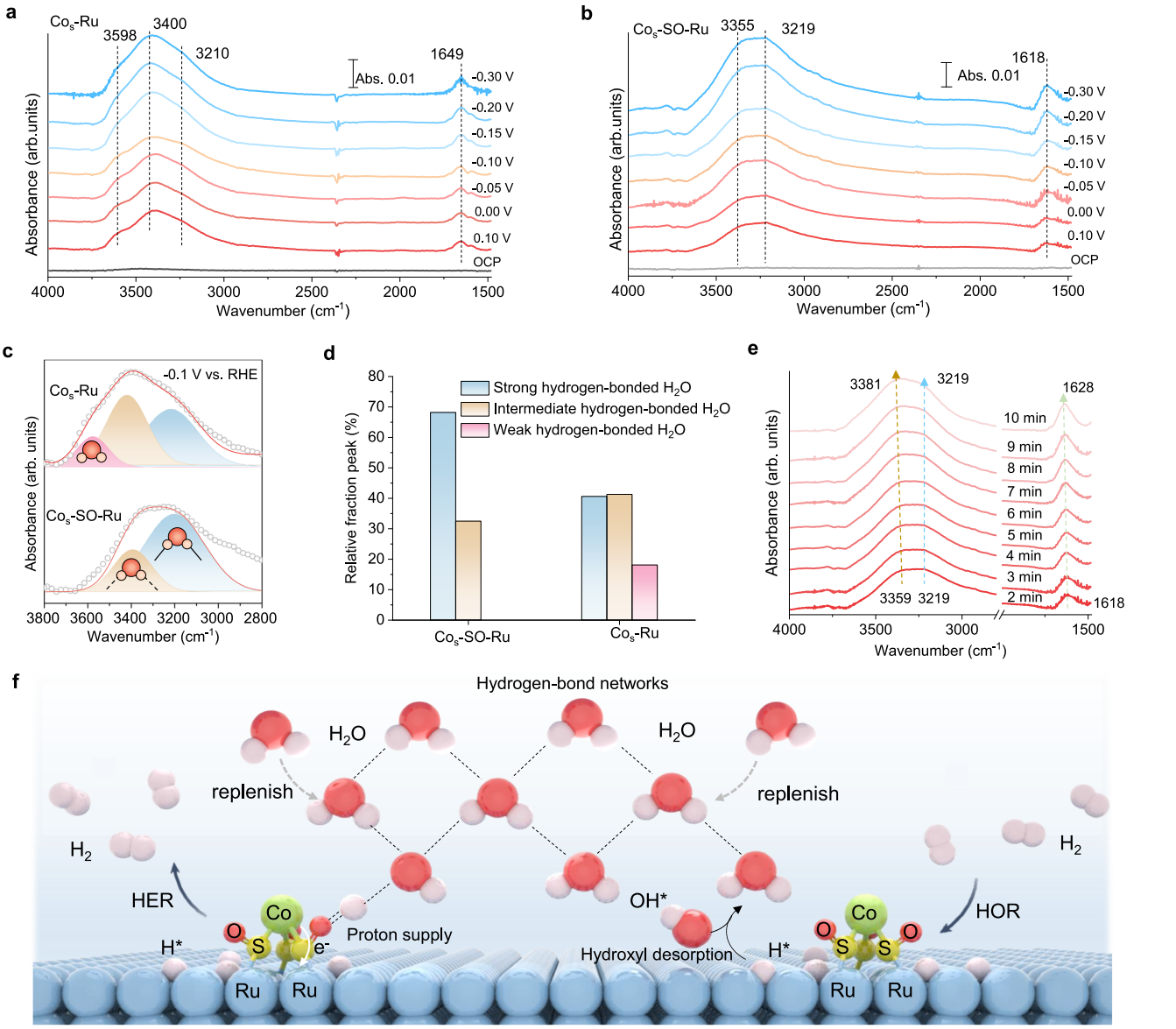

Fig. 5 | Electrocatalytic mechanistic study. In situ ATR-SEIRAS spectra of interfacial H_2O on **a** Co_s-Ru and **b** Co_s-SO-Ru catalysts at different potentials in 0.1 M KOH. **c** The deconvolution of bonded H_2O peak of different catalysts at −0.1 V. **d** The relative fraction of different H_2O configuration. **e** In situ ATR-SEIRAS spectra of Co_s-SO-Ru at −0.1 V with increasing reaction time. **f** The schematic illustration of the dynamic hydrogen-bond network conformations. The dotted lines represent hydrogen bonds. Source data are provided as a Source Data file.

oxygen-free surface for Ru[32]. Therefore, sulfo-oxygen bridges can efficiently regulate interface features to create an optimal microenvironment for electrocatalytic hydrogen conversions.

Discussion

The hydrophilic sulfo-oxygen bridges between cobalt and ruthenium in Co_s-SO-Ru can not only efficiently regulate the electronic structures of Ru nanoclusters but also optimize the interface features of adsorbed water molecules, thus enhancing hydrogen electrocatalysis. The formation of a strong hydrogen-bond network with hydrophilic sulfo-oxygen bridges is crucial for creating favorable interfacial conditions for Ru clusters in alkaline electrolytes in comparison with Co doped Ru clusters (Co_s-Ru). Typically, the hydrogen-bond network of interfacial water would decrease the accumulation of cations at electrode surface, thus benefiting the proton supply and promoting the hydrogen conversion kinetics according to the electrochemical analysis and in situ spectroscopic results. Mechanistic studies suggested that the sulfo-oxygen bridged electron donating Co atomic sites adjust the electronic structure to generate a low oxophilic Ru surface for the optimal adsorption of hydroxyl group (OH*). The synergetic modulation effects for H* and OH* intermediates account for the outstanding catalytic performance of Co_s-SO-Ru. This bioinspired electrocatalyst provides important insights into the critical role of the hydrogen-bond network of interfacial water in electrocatalysis by modulating interface catalytic microenvironments.

Methods

Chemicals and materials

$CoSO_4{\cdot}7H_2O$ (AR 99.9%), $Co(NO_3)_2{\cdot}6H_2O$ (AR 99.9%), 4,4-Bipyridine (>98%), pyridine (>99.8%), ethyl alcohol, methanol, and KOH were purchased from Aladdin Co., Shanghai, China. $RuCl_3$ (98.0% metal basis), commercial Pt/C (20% wt%), and Nafion D520 dispersion (5% w/w in water and 1-propanol) were obtained from Alfa Aesar. Unless otherwise stated, all reagents were used without further purification. The hydroxide exchange membrane (PiperION™ A15, 17 μm thick) and the ionomer were bought from Versogen.

https://doi.org/10.1038/s41467-025-61871-2

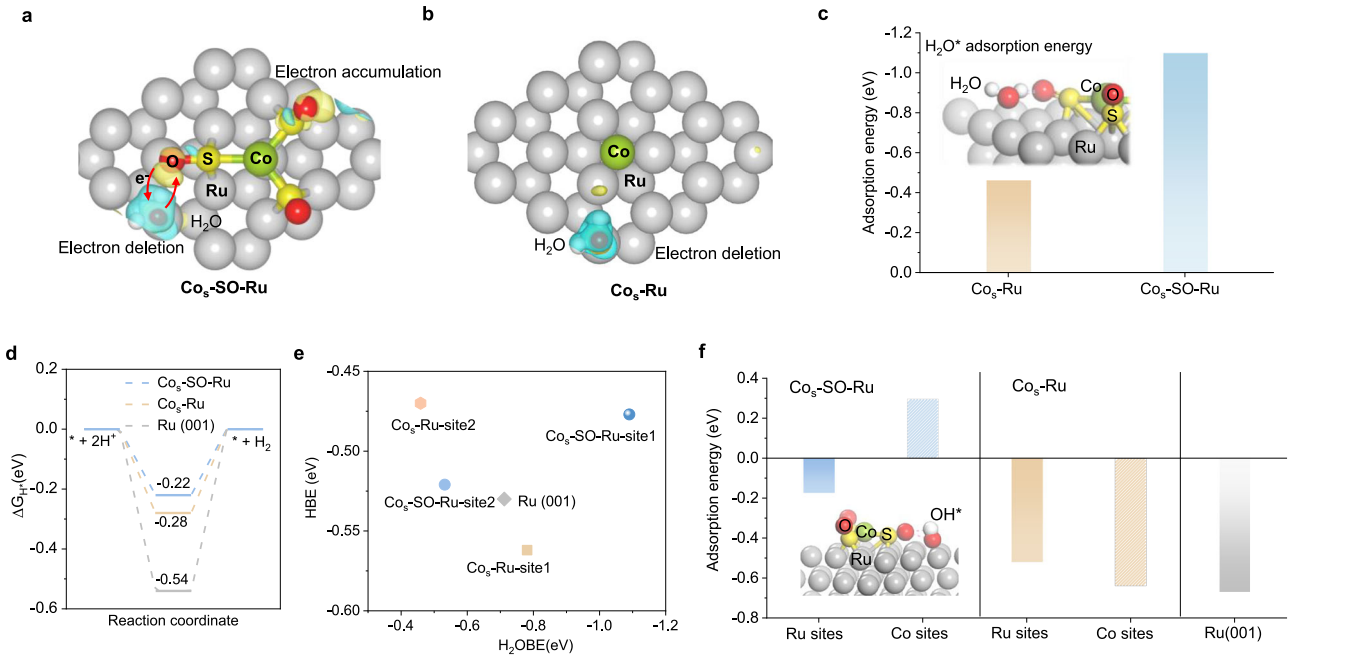

Fig. 6 | Theoretical understanding of the HOR/HER process. The differential charge density image of H_2O adsorbed on **a** Co_s-SO-Ru and **b** Co_s-Ru. The yellow contour indicates electron accumulation, and the cyan contour denotes electron depletion. **c** H_2O^* adsorption energy on different sites. **d** Gibbs free energy diagram of adsorbed H* (ΔG_{H^*}) on different catalytic sites. **e** The HBE and H_2OBE calculated on different catalytic sites. **f** Hydroxyl adsorption energy on different catalytic sites. Source data are provided as a Source Data file.

Synthesis of Co-organic precursor

In a typical procedure, 4 mmol $CoSO_4{\cdot}7H_2O$ was added into 30 mL aqueous solution with 4 mmol 4,4-Bipyridine. Then, 2 mL pyridine and 15 mL ethanol were added dropwise into the above solution under stirring. The mixture was then transferred into a 100 mL Teflon-lined stainless autoclave and heated at 100 °C for another 24 h. The pink precipitates were washed with methanol and ethanol three times and dried at 50 °C. For comparison, the same process was used to prepare the $CoNO_3$-organic precursor by replacing $CoSO_4{\cdot}7H_2O$ with $Co(NO_3)_2{\cdot}6H_2O$.

Synthesis of Co_s-SO-Ru catalysts

Firstly, 15 mg modified Ketjen black was dispersed into 30 mL aqueous solution under vigorously stirring for 24 h at room temperature. The as-prepared Co-organic precursor (45 mg) was added to the mixed solution with ultrasonic treatment for 20 min. Then, the given amount of ruthenium chloride was added to the above mixture and stirred for 8 h at room temperature. Then, the brown precipitates of Co(Ru)-organic precursor with different Ru contents were washed with water and ethanol three times, and dried at 50 °C in the oven. Finally, these obtained powders were thermal treatment in a tube furnace at 500/600/700 °C for 2 h with a ramp rate of 5 °C/min in Ar. The obtained samples were donated as Co_s-SO-Ru-1/2/3, respectively. Subsequently, the Co_s-SO-Ru-etch is prepared via further etching Co_s-SO-Ru in 2 M HCl. If no specific declaration has been made, the Co_s-SO-Ru discussed in the paper refers to Co_s-SO-Ru-2.

Synthesis of Co_s-Ru catalyst

The Co_s-Ru catalyst was synthesized based on the same process as Co_s-SO-Ru, except that the Co-organic precursor was changed to the $CoNO_3$-organic precursor.

Characterizations

Morphological analysis was conducted using a field-emission scanning electron microscope (FE-SEM, Apreo S HiVac, Thermo Fisher Scientific). Surface elemental compositions and electronic structures were probed by X-ray photoelectron spectroscopy (XPS) using a Thermo ESCALAB 250Xi system equipped with a monochromatic Al Kα source. Spectral deconvolution and quantitative analysis were performed with Thermo Avantage software to elucidate the chemical states and metal loadings. X-ray absorption spectroscopy (XAS) data were acquired at beamline BL07A1 of the National Synchrotron Radiation Research Center (NSRRC), employing a Si (111) double-crystal monochromator for photon energy selection. Samples were pressed into uniform pellets and mounted at a normal incidence angle relative to the incoming X-ray beam. The obtained X-ray absorption near-edge structure (XANES) and extended X-ray absorption fine structure (EXAFS) spectra were processed and fitted using the Athena software package. Phase identification and crystallinity were evaluated via powder X-ray diffraction (XRD) using a Rigaku SmartLab diffractometer (9 kW) with Cu Kα radiation, scanned over a 2θ range of 10°–80°. Data interpretation was conducted using MDI Jade and OriginPro software. For atomic-resolution imaging, samples were drop-cast onto lacey carbon-supported copper grids and examined by aberration-corrected scanning transmission electron microscopy (STEM) using a JEOL JEM-ARM 200 F, which incorporates a cold field-emission gun and high-angle annular dark field (HAADF) detector.

Electrochemical measurements

Catalyst inks were prepared by dispersing 10 mg of each catalyst into 1 mL of a Nafion–ethanol solution (prepared by mixing 1 g of 5 wt% Nafion solution with 9 g of ethanol)[56]. The mixture was magnetically stirred until a uniform suspension was obtained. A 5 μL aliquot of the catalyst ink (10 mg mL^{-1}) was then drop-cast onto a glassy carbon electrode (GCE) and dried under ambient conditions, resulting in a catalyst loading of 0.25 mg cm^{-2}. All electrochemical tests were conducted using a Gamry Reference 600 electrochemical workstation (Gamry Instruments, USA) in a standard three-electrode configuration. A reversible hydrogen electrode (RHE) and a graphite rod were employed as the reference and counter electrodes, respectively. A rotating disk electrode (RDE) with a glassy carbon tip (area = 0.196 cm^2) served as the working electrode to evaluate

hydrogen oxidation reaction (HOR) activity. HOR polarization curves were recorded in H_2-saturated 0.1 M KOH electrolyte (pH = 12.9 ± 0.1) at a rotation speed of 1600 rpm and a scan rate of 10 mV s^{-1}. All measurements were automatically corrected for iR drop using real-time resistance compensation (31.0 ohms). Hydrogen evolution reaction (HER) polarization curves were obtained in both Ar-saturated 1.0 M KOH (pH = 13.5 ± 0.1) and simulated alkaline seawater using a sweep rate of 10 mV s^{-1} with iR compensation (4.4 ohms). The simulated seawater was formulated by dissolving 26.73 g NaCl, 2.26 g $MgCl_2$, 3.25 g $MgSO_4$, 1.12 g $CaCl_2$, 0.19 g $NaHCO_3$, 3.48 g Na_2SO_4, and 0.72 g KCl in 1 L of ultrapure water. All electrolytes were freshly prepared and stored in plastic volumetric flasks to avoid contamination.

Electrochemical impedance spectroscopy (EIS) measurements were performed in the frequency range of 100 kHz to 0.1 Hz, applying a 10 mV AC perturbation at a rotation rate of 1600 rpm. The turnover frequency (TOF) was calculated using the equation: TOF = $I/2nF$, where I (A) is the measured current. F is the Faraday constant (96485 C mol^{-1}). $n = m/M$, n (mol) is the molar amount of Ru loaded on the GCE, m is the mass of Ru, and M is the atomic mass. Cyclic voltammetry (CV) for hydrogen underpotential deposition (HUPD) analysis was conducted in Ar-saturated 1.0 M KOH at a scan rate of 50 mV s^{-1}.

The kinetic current density (j_k) was obtained according to the Koutecky-Levich (K-L) equation,

$$\frac{1}{j} = \frac{1}{j_k} + \frac{1}{j_d} \tag{1}$$

where the j, j_k, and j_d are the measured current density, kinetic current density, and diffusion-limit current density, respectively. The HOR is dominated by H_2 diffusion and transport process due to the limited solubility in electrolyte, thus the diffusion-limit current density follows the (K-L) equation as:

$$j_d = BC_0\omega^{\frac{1}{2}} = 0.62nFC_0\left(D_0\right)^{\frac{2}{3}}\nu^{-\frac{1}{6}} \tag{2}$$

where B is the Levich constant, n is the number of transferred electrons, F is the Faraday constant (96,485 C mol^{-1}), C_0 is the solubility of H_2 in electrolyte, D_0 is the diffusivity of H_2 in electrolyte, ν is the kinematic viscosity of the electrolyte.

AEMFCs fabrications and tests

The prepared Cos-SO-Ru or the commercial Pt/C catalysts were utilized as the anode with the loading of 0.1 mg_{metal} cm^{-2}. For cathodic applications, Pt/C catalyst (HiSpec 4000, Alfa Aesar; platinum contents 40 wt%) was deposited with a higher metal loading of 0.4 mgmetallic cm^{-2}. The hydroxide exchange membrane (PiperION™ A15, 17 µm) was used to prepare a catalyst coated membrane (CCM) with the electrode area of 5 cm^{-2}. Additionally, all the CCM were activated by immersed in 3.0 M NaOH overnight. Performance characterization of AEMFCs was conducted using Scribner Associates Model 850-g platform featuring an integrated backpressure regulation assembly.

In situ ATR-SEIRAS

The ATR-SEIRAS was conducted on an FTIR spectrometer with an MCT detector cooled with liquid nitrogen (Nicolet iS50, Bruker). Si crystal prism with chemically deposited Au film is used as conductive substrate for supporting the electrocatalysts. The carbon rod and Ag/AgCl electrodes are employed as counter electrodes and reference electrodes, respectively.

DFT calculations

All electronic structures and adsorption energy calculations were conducted using the CASTEP module within the Materials Studio software suite[57]. The exchange-correlation interactions were treated using the generalized gradient approximation (GGA) with the Perdew–Burke–Ernzerhof (PBE) functional[58,59]. A plane-wave cut-off energy of 450 eV was employed for both atomic and cell optimizations. The simulation cell was defined with dimensions of 11 Å × 11 Å × 28 Å. Brillouin zone sampling was performed using a Monkhorst-Pack grid of 3 × 3 × 1 centered at the k-point for each unit cell. The energy convergence criterion for self-consistent field (SCF) iterations was set to 1.0×10^{-5} eV per atom. Additionally, the maximum allowable stress and displacement were constrained to 0.05 GPa and 0.001 Å, respectively. After structural relaxation, differential charge density analyses were systematically conducted. The equations for calculating adsorption energy ΔE_{H^*}, ΔE_{OH^*} and $\Delta E_{H_2O^*}$ as the following[60]:

$$\Delta E_{H^*} = E_{slab+H} - E_{slab} - \frac{1}{2}E_{H_2}$$

$$\Delta E_{OH^*} = E_{slab+OH} - E_{slab} - \left(E_{H_2O} - \frac{1}{2}E_{H_2}\right)$$

$$\Delta E_{H_2O^*} = E_{slab+H_2O} - E_{slab} - E_{H_2O}$$

where the E_{slab+H}, $E_{slab+OH}$, and E_{slab+H_2O} denote the total energies of the slab with adsorbed of H, OH, and H_2O, respectively. The energy of the catalysts is E_{slab}, and the H_2 and H_2O energy is E_{H_2} and E_{H_2O}. The Gibbs free energy (ΔG) was calculated as follows:

$$\Delta G = \Delta E + \Delta ZPE - T\Delta S$$

where ΔZPE is the change in zero-point energy, T represents the temperature (T = 298.15 K), and ΔS is the entropy change.

Data availability

All relevant data that support the findings of this study are presented in the manuscript and supplementary information file. Source data are provided with this paper.

References

1. Glenk, G. & Reichelstein, S. Economics of converting renewable power to hydrogen. *Nat. Energy* **4**, 216–222 (2019).
2. Fang, J. et al. Atomically dispersed Iridium on Mo2C as an efficient and stable alkaline hydrogen oxidation reaction catalyst. *Nat. Commun.* **15**, 4236 (2024).
3. Zhou, Y. et al. Quantum confinement-induced anti-electrooxidation of metallic nickel electrocatalysts for hydrogen oxidation. *Nat. Energ.* **9**, 1297–1309 (2024).
4. Cheng, R. et al. Rational design of organic electrocatalysts for hydrogen and oxygen electrocatalytic applications. *Adv. Mater.* **36**, 2402184 (2024).
5. Mao, J. et al. Electrochemical lithiation regulates the active hydrogen supply on Ru–Sn nanowires for hydrogen evolution toward the high-performing anion exchange membrane water electrolyzer. *J. Am. Chem. Soc.***147**, 7711–7720 (2025).
6. Shi, Z. et al. Phase-dependent growth of Pt on MoS2 for highly efficient H2 evolution. *Nature* **621**, 300–305 (2023).
7. Zhu, S. et al. The role of ruthenium in improving the kinetics of hydrogen oxidation and evolution reactions of platinum. *Nat. Catal.* **4**, 711–718 (2021).
8. Gao, F.-Y. et al. Nickel–molybdenum–niobium metallic glass for efficient hydrogen oxidation in hydroxide exchange membrane fuel cells. *Nat. Catal.* **5**, 993–1005 (2022).
9. Li, L. et al. Surface and lattice engineered ruthenium superstructures towards high-performance bifunctional hydrogen catalysis. *Energy Environ. Sci.* **16**, 157–166 (2023).

10. Rong, C., Dastafkan, K., Wang, Y. & Zhao, C. Breaking the activity and stability bottlenecks of electrocatalysts for oxygen evolution reactions in acids. *Adv. Mater.* **35**, 2211884 (2023).
11. Yang, J., Zhu, C., Li, W.-H., Zheng, X. & Wang, D. Organocatalyst supported by a single-atom support accelerates both electrodes used in the chlor-alkali industry via modification of non-covalent interactions. *Angew. Chem. Int. Ed.* **63**, e202314382 (2024).
12. Hu, Y. et al. Cooperative Ni(Co)-Ru-P sites activate dehydrogenation for hydrazine oxidation assisting self-powered H_2 production. *Angew. Chem. Int. Ed.* **62**, e202308800 (2023).
13. Dai, S. et al. Low-barrier hydrogen bonds in enzyme cooperativity. *Nature* **573**, 609–613 (2019).
14. Zhou, Y. et al. Lattice-confined Ru clusters with high CO tolerance and activity for the hydrogen oxidation reaction. *Nat. Catal.* **3**, 454–462 (2020).
15. Ding, Y. et al. A monolayer high-entropy layered hydroxide frame for efficient oxygen evolution reaction. *Adv. Mater.* https://doi.org/10.1002/adma.202302860 (2023).
16. Song, X. et al. Improving the hydrogen oxidation reaction rate of Ru by active hydrogen in the ultrathin Pd interlayer. *J. Am. Chem. Soc.* **145**, 12717–12725 (2023).
17. Zhang, B. et al. A strongly coupled Ru–CrOx cluster–cluster heterostructure for efficient alkaline hydrogen electrocatalysis. *Nat. Catal.* **7**, 441–451 (2024).
18. He, Q. et al. Synergic reaction kinetics over adjacent ruthenium sites for superb hydrogen generation in alkaline media. *Adv. Mater.* **34**, 2110604 (2022).
19. Yang, C. et al. Electronic structure-dependent water-dissociation pathways of ruthenium-based catalysts in alkaline H2-evolution. *Small* **19**, 2206949 (2023).
20. Chen, J. et al. Reversible hydrogen spillover in Ru-WO3-x enhances hydrogen evolution activity in neutral pH water splitting. *Nat. Commun.* **13**, 5382 (2022).
21. Zhang, J. et al. Competitive adsorption: reducing the poisoning effect of adsorbed hydroxyl on Ru single-atom site with SnO2 for Efficient hydrogen evolution. *Angew. Chem. Int. Ed.* **61**, e202209486 (2022).
22. Zhao, K. et al. Enhancing hydrogen oxidation and evolution kinetics by tuning the interfacial hydrogen-bonding environment on functionalized platinum surfaces. *Angew. Chem. Int. Ed.* **61**, e202207197 (2022).
23. Liu, E. et al. Interfacial water shuffling the intermediates of hydrogen oxidation and evolution reactions in aqueous media. *Energy Environ. Sci.* **13**, 3064–3074 (2020).
24. Li, P. et al. Hydrogen bond network connectivity in the electric double layer dominates the kinetic pH effect in hydrogen electrocatalysis on Pt. *Nat. Catal.* **5**, 900–911 (2022).
25. Wang, Y.-H. et al. Unraveling stoichiometry effect in nickel-tungsten alloys for efficient hydrogen oxidation catalysis in alkaline electrolytes. *Angew. Chem. Int. Ed.* **63**, e202407613 (2024).
26. Jin, H. et al. Emerging materials and technologies for electrocatalytic seawater splitting. *Sci. Adv.* **9**, eadi7755 (2023).
27. Fan, R. et al. Ultrastable electrocatalytic seawater splitting at ampere-level current density. *Nat. Sustain.* **7**, 158–167 (2024).
28. Ni, W. et al. Synergistic interactions between PtRu catalyst and nitrogen-doped carbon support boost hydrogen oxidation. *Nat. Catal.* **6**, 773–783 (2023).
29. Shen, F. et al. Oxophilic Ce single atoms-triggered active sites reverse for superior alkaline hydrogen evolution. *Nat. Commun.* **15**, 448 (2024).
30. Mu, X. Q. et al. Symmetry-Broken Ru nanoparticles with parasitic Ru-Co Dual-single atoms overcome the volmer step of alkaline hydrogen oxidation. *Angew. Chem. Int. Ed.* **63**, e202319618 (2024).
31. Gan, T. & Wang, D. Atomically dispersed materials: ideal catalysts in atomic era. *Nano Res.* **17**, 18–38 (2024).
32. Sun, Q. et al. Understanding hydrogen electrocatalysis by probing the hydrogen-bond network of water at the electrified Pt–solution interface. *Nat. Energy* **8**, 859–869 (2023).
33. Ji, K. et al. Steering selectivity in electrocatalytic furfural reduction via electrode–electrolyte interface modification. *J. Am. Chem. Soc.* **146**, 11876–11886 (2024).
34. Wang, Y. et al. Strong hydrogen-bonded interfacial water inhibiting hydrogen evolution kinetics to promote electrochemical CO2 reduction to C2+. *ACS Catal.* **14**, 3457–3465 (2024).
35. Wang, T. et al. Enhancing oxygen reduction electrocatalysis by tuning interfacial hydrogen bonds. *Nat. Catal.* **4**, 753–762 (2021).
36. Chen, S. et al. Coordination modulation of hydrated zinc ions to enhance redox reversibility of zinc batteries. *Nat. Commun.* **14**, 3526 (2023).
37. Li, P. et al. Corrosion resistant multilayered electrode comprising Ni_3N nanoarray overcoated with NiFe-Phytate complex for boosted oxygen evolution in seawater electrolysis. *Adv. Energy Mater.* **14**, 2303360 (2023).
38. Buller, R. et al. From nature to industry: harnessing enzymes for biocatalysis. *Science* **382**, eadh8615 (2023).
39. Yokochi, Y., Fukushi, Y., Wakabayashi, K. -i, Yoshida, K. & Hisabori, T. Oxidative regulation of chloroplast enzymes by thioredoxin and thioredoxin-like proteins in Arabidopsis thaliana. *Proc. Natl. Acad. Sci. USA* **118**, e2114952118 (2021).
40. Hardt, S. et al. Reversible H2 oxidation and evolution by hydrogenase embedded in a redox polymer film. *Nat. Catal.* **4**, 251–258 (2021).
41. Dutta, A., Appel, A. M. & Shaw, W. J. Designing electrochemically reversible H2 oxidation and production catalysts. *Nat. Rev. Chem.* **2**, 244–252 (2018).
42. Shi, S. et al. Selective hydrogenation via precise hydrogen bond interactions on catalytic scaffolds. *Nat. Commun.* **14**, 429 (2023).
43. Cao, S. et al. A Library of ROS-catalytic metalloenzyme mimics with atomic metal centers. *Adv. Mater.* **34**, 2200255 (2022).
44. Sun, Y. et al. Catalase-mimetic artificial biocatalysts with Ru catalytic centers for ROS elimination and stem-cell protection. *Adv. Mater.* **34**, 2206208 (2022).
45. Cao, X. et al. Strong p-d orbital hybridization on bismuth nanosheets for high performing CO2 Electroreduction. *Adv. Mater.* **36**, 2309648 (2024).
46. Zheng, X. et al. Dual-atom support boosts nickel-catalyzed urea electrooxidation. *Angew. Chem. Int. Ed.* **62**, e202217449 (2023).
47. Shu, X., Tan, D., Wang, Y., Ma, J. & Zhang, J. Bimetal-bridging nitrogen coordination in carbon-based electrocatalysts for ph-universal oxygen reduction. *Angew. Chem. Int. Ed.* **63**, e202316005 (2024).
48. Yuan, Q. et al. Single-site palladium on sulfur-doped carbon for olefin alkoxycarbonylation: performance determined by coordination environments. *Chem. Catal.* **4**, 100830 (2024).
49. Yang, C. et al. Electron-donating Cu atoms induced high proton supply and anti-poisoning ruthenium clusters for superior direct seawater hydrogen production. *Adv. Funct. Mater.* **34**, 2404061 (2024).
50. Wang, L. et al. The reformation of catalyst: from a trial-and-error synthesis to rational design. *Nano Res.* **17**, 3261–3301 (2024).
51. Yang, X., Nash, J., Oliveira, N., Yan, Y. & Xu, B. Understanding the pH dependence of underpotential deposited hydrogen on platinum. *Angew. Chem. Int. Ed.* **58**, 17718–17723 (2019).
52. Kong, K. et al. Electrochemical carbon–carbon coupling with enhanced activity and racemate stereoselectivity by microenvironment regulation. *Nat. Commun.* **14**, 6925 (2023).
53. Zhu, S. et al. Reconstructing hydrogen-bond network for efficient acidic oxygen evolution. *Angew. Chem. Int. Ed.* **63**, e202319462 (2024).

54. Tang, T. et al. Unconventional bilateral compressive strained Ni–Ir interface synergistically accelerates alkaline hydrogen oxidation. *J. Am. Chem. Soc.* **145**, 13805–13815 (2023).
55. Qiu, Z. et al. 2D MOF-assisted pyrolysis-displacement-alloying synthesis of high-entropy alloy nanoparticles library for efficient electrocatalytic hydrogen oxidation. *Angew. Chem. Int. Ed.* **62**, e202306881 (2023).
56. Wu, H. et al. Alkaline-earth-metal regulated metal carbides with bioinspired gradientOH spillover for efficient and long-lasting direct seawater electrolysis. *J. Mater. Chem. A* **12**, 10755–10763 (2024).
57. Clark, S. J., et al. First principal methods using CASTEP. *Zeitschrift für kristallographie-crystalline Mater.* **220**, 567–570 (2005).
58. Perdew, J. P., Burke, K. & Ernzerhof, M. Generalized gradient approximation made simple. *Phys. Rev. Lett.* **77**, 3865–3868 (1996).
59. Hasnip, P. J. & Pickard, C. J. Electronic energy minimisation with ultrasoft pseudopotentials. *Comput. Phys. Commun.* **174**, 24–29 (2006).
60. Yang, C. et al. Mn-oxygen compounds coordinated ruthenium sites with deprotonated and low oxophilic microenvironments for membrane electrolyzer-based H_2-production. *Adv. Mater.* **35**, 2303331 (2023).

Acknowledgements

This work was financially supported by the National Natural Science Foundation of China (22175108, 22409123 & 22379086), the Natural Science Foundation (ZR2022ZD27, ZR2024QB113) of Shandong Province, Taishan Scholars Program (No. tstp20221105) of Shandong Province, China Postdoctoral Science Foundation (2024M761783), and Postdoctoral Fellowship Program of CPSF (GZC20231443). The authors also acknowledge the assistance of the Analytical Center for Structural Constituent and Physical Property of Core Facilities Sharing Platform (Shandong University), Center for Microscopy and Analysis (Nanjing University of Aeronautics and Astronautics), and the 1W1B station in the BSRF and the BL11B station in the SSRF for help with XAS characterizations. We gratefully acknowledge professor Zhongbin Zhuang at Beijing University of Chemical Technology for their assistance in the AEMFCs tests and analytical support.

Author contributions

C.D.Y., G.Y., C.C., D.S.W., and J.T.Z. proposed the idea and designed the experiments. Y.Q.W., S.L., Z.C.Z, and Y.J.Z. helped with the electrochemical experiments and results analysis. Z.Y.X, X.X.S., S.L., and G.Y. design and conduct the theoretical calculations. C.D.Y., G.Y., and J.T.Z. wrote and edited the manuscript. C.C., D.S.W., and J.T.Z. supervised the whole project. All authors discussed the results and commented on the manuscript.

Competing interests

The authors declare no competing interests.

Additional information

Supplementary information The online version contains supplementary material available at https://doi.org/10.1038/s41467-025-61871-2.

Correspondence and requests for materials should be addressed to Chong Cheng, Dingsheng Wang or Jintao Zhang.

Peer review information *Nature Communications* thanks Ramesh Singh and the other anonymous reviewer(s) for their contribution to the peer review of this work. A peer review file is available.